

# Analysis of astronomical data from optical superconducting tunnel junctions

J.H.J. de Bruijne, A.P. Reynolds, M.A.C. Perryman, F. Favata, A. Peacock

*Astrophysics Division, Space Science Department of ESA, ESTEC, P.O.Box 299, NL-2200 AG Noordwijk, the Netherlands;  
jdbruijn@astro.estec.esa.nl*

Accepted for publication in: *Focal plane detector array developments*, eds Z. Ninkov, W.J. Forrest, Optical Engineering (The International Society for Optical Engineering; SPIE), scheduled for publication in December 2001.

Currently operating optical superconducting tunnel junction (STJ) detectors, developed in ESA, can simultaneously measure the wavelength ( $\Delta\lambda = 50$  nm at 500 nm) and arrival time (to within  $\sim 5$   $\mu$ s) of individual photons in the range 310–720 nm with an efficiency of  $\sim 70\%$ , and with count rates of order 5 000 photons per second per junction. A number of STJ junctions placed in an array format generates four-dimensional data: photon arrival time, energy, and array element ( $X, Y$ ). Such STJ cameras are ideally suited for, e.g., high time-resolution spectrally-resolved monitoring of variable sources or low-resolution spectroscopy of faint extragalactic objects.

The reduction of STJ data involves detector efficiency correction, atmospheric extinction correction, sky background subtraction, and, unlike that of data from CCD-based systems, a more complex energy calibration, barycentric arrival time correction, energy range selection, and time binning; these steps are, in many respects, analogous to procedures followed in high-energy astrophysics. This paper discusses these calibration steps in detail using a representative observation of the cataclysmic variable UZ Fornacis; these data were obtained with ESA's S-Cam2  $6 \times 6$ -pixel device. We furthermore discuss issues related to telescope pointing and guiding, differential atmospheric refraction, and atmosphere-induced image motion and image smearing ("seeing") in the focal plane. We also present a simple and effective recipe for extracting the evolution of atmospheric seeing with time from any science exposure, and discuss a number of caveats in the interpretation of STJ-based time-binned data, such as light curves and hardness ratio plots.

Key words: Astronomy; Data processing; Detectors; Focal plane arrays; Spectro-photometers; Superconducting tunnel junction

## 1. Introduction

Superconducting tunnel junctions (STJs) are powerful photon counting detectors. Since the energy gap between the ground state and the first excited state of an STJ is only a few meV (compared to a band gap of  $\sim 1$  eV for a semi-conductor such as silicon), an individual optical photon, with an energy of order a few eV, has the ability to free a large number of charge carriers, in proportion to its energy, when hitting an STJ. Measuring the resulting electrical pulse allows for an accurate and simultaneous determination of the photon arrival time and energy.

A number of STJs placed in an array format provides a superconducting tunnel junction camera (S-Cam). Such an instrument is currently being developed within the Astrophysics Division of the Space Science Department of ESA (e.g., Peacock et al. 1997, 1998; Verhoeve et al. 2001, in this volume). The presently operating prototype, S-Cam2, has seen a successful series of technical validation and science qualification runs at the 4.2 m William Herschel Telescope (WHT) on La Palma.

S-Cam2 consists of a staggered  $6 \times 6$  array of Tantalum STJs measuring  $25 \times 25$   $\mu\text{m}^2$  each (Figure 1). Inter-junction dead spaces measure  $\sim 4$   $\mu\text{m}$ , resulting in a filling factor of  $\sim 0.78$ . In the focal plane, each junction corresponds to  $\sim 0.6'' \times 0.6''$  on the sky; the entire field of view of S-Cam2 is  $\sim 4'' \times 4''$ . The focal plane array is directly illuminated from the f/11 Nasmyth 1 focus of the telescope, without loss of angular resolution, through dedicated collimating optics and a lateral optical window. The array operates at  $\sim 0.32$  K, well below the critical temperature of Tantalum (4.48 K) in a sophisticated cryogenic environment; instrumental dark current, the amplitude of which depends on the detector temperature and on any residual infrared stray radiation, is negligible (Verhoeve et al. 2001). The photon-generated electrical pulses are read out using charge-sensitive amplifiers operating at room temperature; S-Cam2,

being a photon-counting detector, does not suffer from read-out noise. A dedicated data acquisition computer stores the observations, in real time, in a 4-column event-list format: photon arrival time, energy, and array element ( $X, Y$ ).

Whereas the intrinsic speed of a Tantalum STJ is typically below  $\sim 1$  ns, S-Cam2 photon arrival time stamps are accurate to within  $\sim 5$   $\mu$ s with respect to GPS timing signals; this accuracy level is set by the present signal processing electronics. S-Cam2 has a count rate limitation of  $\sim 5\,000$  photons  $\text{s}^{-1}$  per junction and  $\sim 30\,000$  photons  $\text{s}^{-1}$  for the entire device; these limits are also set by the present electronics and real-time processing software. The spectral resolving power  $\lambda/\Delta\lambda$  of an STJ increases with the square root of the photon energy. The intrinsic wavelength resolution, the so-called Fano limit, of Tantalum is  $\Delta\lambda \sim 12$  nm at  $\lambda = 500$  nm. The corresponding value for S-Cam2 is  $\sim 60$  nm at 500 nm; this value is mainly set by two, roughly equally important, components: the electronics and the thermal infrared background radiation from the telescope and atmosphere. Although the intrinsic wavelength response of Tantalum is very broad (from shortward of 300 nm to longward of 2 000 nm), the response of S-Cam2 is restricted to  $\sim 310$ – $720$  nm. The blue limit is predominantly set by the Earth’s atmosphere. In order to reduce thermal noise photons, all low-energy (i.e., red) photons are deliberately suppressed by means of a series of optical filter elements.

The photon detection efficiency (“quantum efficiency”) of S-Cam2 is  $\sim 60$ – $70\%$  over the range 310–720 nm; it is mainly determined by the properties of the substrate (sapphire) on which the back-illuminated STJs are deposited. The total throughput of the S-Cam2 optical system, including the WHT primary and secondary mirrors ( $\sim 85\%$  transmission each), the Nasmyth flat ( $\sim 85\%$  transmission) and optical derotator ( $\sim 50\%$  transmission), the S-Cam2 optics ( $\sim 25\%$  transmission), and the detection efficiency ( $\sim 70\%$ ), is a few per cent over this range.

The high detection efficiency, broad energy response, and high speed of STJ cameras, combined with their inherent energy resolution and photon counting capabilities, make these instruments ideally suited to perform, e.g., high time-resolution energy-resolved photometry of variable sources (e.g., Perryman et al. 2001) or low-resolution spectroscopy of faint objects (“photometric redshifts”; e.g., Perryman et al. 1993; Jakobsen 1999; Mazin et al. 2000). S-Cam2 observations of a variety of astronomical objects, such as  $\gamma$ -ray bursts, cataclysmic variables, pulsars, and dwarf novae, are currently being analyzed in detail. Future investigations will use S-Cam data to deepen the study of the characteristics of atmospheric seeing and scintillation, touching upon topics such as speckle imaging and spectroscopy, adaptive optics, and interferometric fringe detection.

STJ cameras are complex systems, both from the manufacturing and the operational point of view (see, e.g., Verhoeve et al. 2001 for a detailed discussion). Moreover, the four-dimensional data cube generated by STJ detectors provides new challenges regarding data reduction and analysis as compared to normal CCD procedures, although general experience and procedures built up in and developed for the field of high-energy astrophysics have proven highly useful. This contribution addresses some of these aspects by using a representative S-Cam2 observation of the cataclysmic variable UZ For as a working example. Astrophysical results of this and other S-Cam2 exposures will be presented elsewhere.

## 2. Reduction and calibration

S-Cam data are stored, in conventional binary FITS format, as event lists, containing for each detected photon a spatial location (array element  $X, Y$  in the range 1–6, 1–6), arrival time, and energy channel (in the range 0–255). Prior to scientific analyses, raw S-Cam data are fed through an automated pipeline. This software performs a pixel-dependent energy calibration, a photon time stamp correction (when referring to the Solar system barycentre), a pixel-dependent detection efficiency correction (“flat fielding”), an energy-dependent atmospheric extinction correction, and a sky background subtraction. The following subsections summarize each of these steps, using an exposure representative of the characteristics and capabilities of S-Cam2 as an example. This observation, of the eclipsing binary system UZ Fornacis consisting of a white dwarf and a main sequence star, was taken on October 4, 2000, 04:30:41–05:00:41 UTC under moderate seeing conditions ( $\sim 1''$ ; §4F). During the exposure, UZ For’s zenith angle evolved from  $z = 55.19^\circ$  to  $56.78^\circ$ , i.e., the airmass  $A$  changed from 1.75 to 1.83. The 1 800-s frame captures, at roughly mid-exposure, a  $\sim 480$  s eclipse of the bright white dwarf. During this event, the relatively faint reddish contribution from the low-mass companion star remains visible (§4B; cf. Reynolds 2001).

## A. Energy calibration

Incident photons of energy  $E_{\text{photon}}$  are assigned to energy channels  $E_i = i$ , where  $i = 0, \dots, 255$ . Laboratory measurements using a tunable monochromatic light source (325–725 nm) confirm that all 36 S–Cam2 junctions have a highly linear, yet slightly pixel-dependent, energy response:

$$E_i^j = G^j \cdot E_{\text{photon}} + C^j, \quad (1)$$

where  $G^j$  (in channels per eV) is the gain and  $C^j$  (in channels) the corresponding offset of pixel  $j$ . We have implemented the energy calibration of S–Cam2 in two steps. First we correct for the inter-pixel differences by bringing the gain and offset of all pixels to that of an arbitrary reference pixel ( $X, Y = 3, 1$  in this case). We then assign an absolute energy (or wavelength) calibration to this reference pixel.

As the monochromator is a non-portable device, the exact values and temporal stability of the different gains and offsets during an observing campaign can only be obtained and monitored by using a red LED as a semi-monochromatic secondary light source ( $\lambda = 650$  nm at room temperature). When operating this LED at a sufficiently high photon flux, two (or  $n$ ) equal-energy LED photons arriving simultaneously, i.e., within a few  $\mu\text{s}$  of each other, are detected as one event with twice (or  $n$  times) the single LED photon energy. An LED spectrum thus consists of a primary peak, corresponding to 650 nm photons, and a number of higher-order photon peaks at multiple energies of a single LED photon. In practice, only two higher-order peaks are detected in all pixels, of which only the first one is strong enough to be used. By measuring the centroids of these two peaks,  $E_{\text{peak } 1}^j$  and  $E_{\text{peak } 2}^j$ , for each pixel  $j$ , the observed energies  $E_i^j$  of all detected photons can be brought to a common reference scale, corresponding to pixel ( $X, Y = 3, 1$ ), according to:

$$E_i^j \rightarrow \text{NINT} \left( E_{\text{peak } 1}^{(3,1)} + \frac{E_{\text{peak } 1}^{(3,1)} - E_{\text{peak } 2}^{(3,1)}}{E_{\text{peak } 1}^j - E_{\text{peak } 2}^j} \cdot \left( E_i^j - 0.5 + \text{RAN} - E_{\text{peak } 1}^{(3,1)} \right) \right), \quad (2)$$

where RAN is a random deviate between 0 and 1, and the function NINT rounds to the nearest integer. The term “ $-0.5 + \text{RAN}$ ”, which is a random number between  $-0.5$  and  $+0.5$ , has been included, following normal practice in high-energy astrophysics analyses (e.g., Hasinger & Snowden 1990), in order to avoid a repetitive pattern of “spikes” and/or “dips” in the gain-corrected energy channel distributions (the energy resolution decrease resulting from this step is negligible).

The absolute calibration of the reference pixel can be established by using the laboratory-based monochromator data as well as the LED exposures taken throughout the observing campaign (the calibration is somewhat complicated in practice as a result of the presence of a small but significant dependence of the LED photon energy with ambient temperature). These methods provide consistent results,  $G^{(3,1)} \sim 42.5$  and  $C^{(3,1)} \sim -2.0$ , confirming the high temporal stability of the detector. The final (pixel-independent) relation between (gain-corrected) energy channel  $E_i = i$  ( $i = 0, \dots, 255$ ) and photon wavelength  $\lambda$  thus becomes:

$$\lambda \text{ [nm]} = \frac{1239.75 \cdot G^{(3,1)}}{E_i - C^{(3,1)}} = \frac{52689.4}{E_i + 2.0}, \quad (3)$$

where 1239.75 is the conversion factor between photon wavelength  $\lambda$  [nm] and energy  $E$  [eV].

## B. Barycentric time stamp correction

Photon arrival times are stored in UTC (Universal Coordinated Time). However, studies of time-dependent targets such as binary systems or pulsars often require arrival times with respect to the Solar system barycentre (TDB, Barycentric Dynamical Time). The pipeline processing therefore optionally modifies UTC time stamps to TDB values. It does so by going from UTC to TAI (International Atomic Time; +32 s at the observation epoch of UZ For), from TAI to TDT (Terrestrial Dynamical Time; +32.184 000 s), and from TDT to TDB. The last step requires knowledge of the right ascension and declination of the object at the observation epoch and the geographic longitude, latitude, and altitude of the telescope to correct for the observer’s location on and the diurnal motion of the Earth.

Our software uses the JPL DE200 ephemeris to track the location of the Earth with respect to the Solar system barycentre during the observation, taking propagation delay in space–time, caused by the presence of the Sun, into account. For UZ For, the final corrections applied to the arrival time stamps vary from +369.799 990 s for the first to +369.865 824 s for the last photon.

### C. Energy range selection

In the next step, the photon stream is split into a number of energy-selected ranges. This is useful for rapid diagnostic purposes and allows for the construction of, e.g., colour–colour and hardness ratio plots (§4 B). The pipeline software generates, on the basis of the shape of the underlying source spectrum, a user-defined number of energy bands, so that (roughly) equal numbers of events are contained in each of them. The default number of ranges is presently  $n = 3$  (given the limited energy resolution of S–Cam2), which are loosely referred to here as “red”, “yellow”, and “blue”. For the case of UZ For, the low-energy band is  $E_0$ – $E_{98}$  (red), the medium-energy band is  $E_{99}$ – $E_{116}$  (yellow), and the high-energy band is  $E_{117}$ – $E_{255}$  (blue; cf. Table 1). From now on, all calibration steps are performed on the data file containing all counts (energy band 0) as well as on the  $n$  energy-selected sub-exposures.

### D. Time binning

The remaining calibration steps (detection efficiency correction, atmospheric extinction correction, and sky background subtraction) are intricate to introduce and deal with at the individual photon level. The pipeline software therefore introduces an *a posteriori* time binning of the data, based on a user-specified time interval. This interval can, in principle, be arbitrarily small or large, and should be defined taking into account the specific scientific question which is to be addressed. For the UZ For data discussed here, we adopt a 1-s binning. Figure 1 shows the resulting pixel-selected light curves at this stage (cf. §4 B).

### E. Detection efficiency correction (“flat fielding”)

The detection efficiency of an S–Cam pixel is, in principle, a function of time, the incident-photon energy, and the pixel number. The latter dependency results from intrinsic pixel-to-pixel differences as well as vignetting effects related to the relay optics including the infrared photon blocking filters. Laboratory measurements have shown that detection efficiency variations are largely time- and energy-independent, so that, in practice, the usage of a single “flat field map” is adequate.

We therefore choose, in order to correct for pixel-to-pixel efficiency variations, to apply a differential correction, relative to an arbitrary reference pixel ( $X, Y = 3, 1$  in this case), to the time-binned count rates (“exposure time correction” in high-energy astrophysics jargon). Figure 2 shows a correction map which is based on 18 sky observations obtained during the third S–Cam2 campaign (Sep–Oct 2000). Its smooth structure is most likely explained in terms of vignetting, suggesting that intrinsic pixel-to-pixel variations are probably small.

### F. Atmospheric extinction correction

In the optical part of the spectrum, atmospheric extinction is a function of wavelength as a result of dust scattering and of Rayleigh scattering and absorption by air molecules (e.g., Hayes et al. 1975). Furthermore, extinction is zenith angle- and thus pointing- and time-dependent. It is therefore important to correct for this effect. Atmospheric extinction affects the ground-based observed magnitude  $V_\lambda$  “at wavelength  $\lambda$ ” of a celestial object according to:

$$V_\lambda = V_{0,\lambda} + k_\lambda \cdot A, \tag{4}$$

where  $V_{0,\lambda}$  is the object’s magnitude above the Earth’s atmosphere,  $k_\lambda = 1.086 \cdot \tau_0$  [mag airmass<sup>−1</sup>] is the extinction coefficient,  $\tau_0 > 0$  is the optical depth of the atmosphere at zenith angle  $z = 0^\circ$  ( $A = 1$ ), and  $A \sim \sec(z) = \cos^{-1}(z)$

is the airmass<sup>1</sup>.

It is customary, partly because more rigorous options are impractical, to correct for extinction by using time-averaged extinction coefficients. Although extinction can vary from night to night and from season to season, mainly due to a varying contribution from dust scattering (but see Stickland et al. 1987), the pipeline software uses mean coefficients  $k_\lambda$  ( $\lambda = 300\text{--}1100$  nm) valid for La Palma (King 1985). For each energy band, the wavelength corresponding to the centroid energy channel is calculated according to equation 3, after which  $k_\lambda$  is determined using a linear interpolation in the La Palma table. The time-binned count rates are subsequently multiplied by  $10^{0.4k_\lambda \cdot A}$ . Table 1 summarizes this calibration step for the UZ For exposure discussed here.

## G. Background subtraction

In the optical part of the spectrum, the main contributions to the intensity of the night sky are, in order of decreasing importance, the Moon (e.g., Krisciunas et al. 1991), airglow, and zodiacal light (e.g., Benn et al. 1998; Leinert et al. 1998). As a result, the night sky brightness is dependent on pointing, and, as a consequence, on time<sup>2</sup>. The time variability is, however, generally negligibly small when tracking an object on time scales of tens of minutes, except when observing during a Moon-rise or -set<sup>3</sup>.

An optimum background subtraction, i.e., source extraction, for S-Cam data requires the construction of a “spatial source mask”. This is a non-trivial exercise, as atmospheric seeing affects both the size and the location of the point spread function on time scales of ms (e.g., Coulman 1985; cf. §4F). The location of such a source mask is, moreover, energy-dependent as a result of differential atmospheric refraction (§4D). As a first step, we have therefore implemented a simplified background subtraction procedure.

The S-Cam data reduction software, by default, applies a time-independent background subtraction, and optionally allows for a time-dependent sky brightness determination. Under normal atmospheric seeing, telescope guiding, and image centering conditions, the corner pixels ( $X, Y = 1, 1$ ) and (6, 6) are, as a result of the S-Cam2 device architecture, most suitable for a determination of the sky background intensity (e.g., Figure 1). The bottom panels of Figure 3 show, for the Moon-less UZ For exposure, the light curves of these two pixels at the selected binning period (1 s; §4B). These junctions clearly provide a robust estimate of the sky brightness. The default procedure therefore is to subtract, from the pixel-selected light curves, the mean value of the time-averaged count rates of the two corner pixels ( $\sim 26.5$  counts  $\text{s}^{-1}$  pixel $^{-1}$  in this case); the time-dependent option subtracts the mean value of the time-binned count rates, although subtracting a smoothly varying function fitted to the time-binned count rates has the advantage that the signal-to-noise ratio of the resulting light curve is not degraded unnecessarily. The top panel of Figure 3 shows the pixel-integrated sky-subtracted light curve of UZ For (all energies; cf. Figure 4).

## 3. Light curve interpretation

The light curves of UZ For displayed, e.g., in Figure 3 show a rich structure. Before attributing this structure to physical properties of the observed source, it is important to address a number of potential caveats in the interpretation of STJ-based time-binned data. Whereas some of these caveats are well known and common to the general field of aperture photometry (e.g., Mighell 1999), others are specific to S-Cam observations.

---

<sup>1</sup> This formula is based on the plane parallel layer approximation for the atmosphere. The pipeline software uses an extended formula, which is also valid at large zenith angles ( $z \gtrsim 80^\circ$ ):  $A = \sec(z) - 0.0018167 \cdot (\sec(z) - 1) - 0.0028750 \cdot (\sec(z) - 1)^2 - 0.0008083 \cdot (\sec(z) - 1)^3$ .

<sup>2</sup> Intrinsic variability is driven by, e.g., the amount of dust in the atmosphere and the phase of the Solar activity cycle.

<sup>3</sup> A time-variable background intensity can also result from telescope-induced guiding motions when observing, e.g., objects superimposed on extended extragalactic sources, or objects embedded in a spatially non-uniform nebulosity (e.g., the Crab pulsar).

## A. Photon noise and atmospheric scintillation

A fundamental limit to the precision with which the brightness of any celestial object can be measured is set by Poissonian photon noise. The “flat-fielded” and sky-subtracted light curve of UZ For (e.g., Figure 3) has, outside eclipse, a count rate of  $\sim 2000$  counts per 1-s time bin. The correspondingly expected Poisson noise is  $\sqrt{2000} = 45$  counts  $\text{s}^{-1}$ , i.e.,  $\sim 2.2\%$ .

Atmospheric scintillation (the rapidly varying turbulent refocussing of light rays passing through the atmosphere) is a second random noise contributor beyond the control of the observer. For integration times of order  $\sim 1$  s or longer, the root-mean-square deviation of the relative intensity of star light due to (the low-frequency component of) scintillation is given by (e.g., Young 1967; Young et al. 1991; Dravins et al. 1998):

$$\sim 0.09 \left( \frac{D}{1 \text{ cm}} \right)^{-2/3} \cos^{-7/4}(z) \exp\left(-\frac{L}{L_0}\right) \left( \frac{2 T}{1 \text{ s}} \right)^{-1/2} \sim 0.2\%, \quad (5)$$

where  $D = 4.2$  m,  $z \sim 56^\circ$ ,  $L_0 = 8000$  m is the pressure scale height of the atmosphere,  $L = 2332$  m is the altitude of the aperture above sea level, and  $T = 1$  s is the integration time (of a single time bin in this case). We thus conclude that Poisson noise is the dominant random noise term. This is generally true for a 1-s time binning: scintillation starts dominating Poisson noise at the WHT when receiving more than  $\sim 1\,391\,000/123\,000$  photons  $\text{s}^{-1}$  from a source at zenith angle  $z = 0^\circ/60^\circ$  (recall that S-Cam2 can “only” handle count rates up to  $\sim 30\,000$  photons  $\text{s}^{-1}$  due to electronic limitations).

## B. Caveats related to image motion

Atmospheric seeing is known to affect both the size and the location of the point spread function at time scales of ms (e.g., Coulman 1985; cf. §4 F). This is clearly demonstrated by the pixel-selected light curves displayed in Figure 1. Image motion (§4 E), either due to atmospheric seeing or due to guiding and tracking errors and corrections (cf. §4 G), may lead to spurious effects in, e.g., (energy-selected) light curves and hardness ratio plots (§4 B) for at least three reasons.

First of all, possibly uncorrected spatial variations in the detection efficiency (§2 E) can induce spurious light curve effects in the event that the image moves around in the focal plane.

A second caveat is formed by the inter-junction dead spaces (§1). These gaps cause, as the image moves over the array, a time-dependent flux loss leading to a more-or-less random noise component in the light curves. Simulations show that the photometric scatter introduced by this effect is negligibly small ( $\ll 1\%$ ) for typical seeing and image wander conditions; only in the rare case the seeing is better (smaller) than the size of an individual pixel, i.e.,  $\sim 0.60''$ , the effect of the dead zones can be significant (up to a few per cent). It is, in principle, possible to partially correct for this effect in the data reduction process, although the adequacy of the correction depends on the knowledge of the instantaneous motion and form of the point spread function.

A third hazard is the image smearing component of atmospheric seeing. Periods of poor seeing are characterized by a large point spread function (full width at half maximum up to several arcseconds), the extended wings of which may contain a significant fraction of the total flux. Whereas such a configuration may already lead to a loss of light beyond the detector boundary, the additional presence of image motion can lead to significantly spurious light curve effects. These effects are (potentially) energy-dependent as a result of atmospheric dispersion (§4 D). An additional complication is posed by the fact that poor seeing may, also depending on the brightness of the object, place a significant number of source photons, compared to the sky background, on the corner pixels ( $X, Y = 1, 1$ ) and  $(6, 6)$  which are used for sky subtraction (cf. Figure 3). Due to the complexity of this process, an *a posteriori* correction for these effects (similar to an “aperture correction” that is normally applied in stellar photometry; e.g., Stetson 1990) is hardly feasible. The effects of poor seeing can only be compensated for by brute force, i.e., a larger focal-plane array.

## 4. S-Cam data products

## A. Event-list data

A key feature of S-Cam is its photon-counting ability. As a result, the most rudimentary output of the pipeline processing is a gain-corrected (and possibly barycentre-corrected) event list. Although such data are potentially cumbersome to process and interpret, knowledge of photon arrival times can be important, e.g., for high-precision ephemeris studies or timing of light pulses (Delamere 1992; Perryman et al. 1999). Furthermore, the (partially) processed event-list data allows the user to inspect and analyze the observations at different time resolutions.

## B. Pixel- and energy-selected time-binned data

Pixel- and energy-selected light curves are valuable for assessing the performance of S-Cam2 and its data reduction software, in addition to the astrophysical interpretation.

UZ For, the object discussed in this paper, is a cataclysmic variable: a spatially unresolved eclipsing binary system composed of a white dwarf and a low-mass main-sequence star filling its Roche lobe, in which the highly magnetic degenerate object accretes material from its mass-losing companion. During the 2 hour orbital period, the bright bluish white dwarf is eclipsed for  $\sim 8$  minutes by the reddish main-sequence star. This event is clearly seen in our data (e.g., Figure 1; cf. Reynolds 2001). Figure 4 shows the “flat-fielded” and sky-subtracted pixel-integrated light curves of UZ For in the energy bands red (“R”), yellow (“V”), and blue (“B”; §2 C). (Although these bands were defined initially such that they contain (roughly) equal amounts of counts (§2 C), the subsequently applied atmospheric extinction correction (§2 F), which is stronger in the blue than in the red, has led to a significantly uneven distribution of counts in the resulting pipeline product.) During the eclipse of the white dwarf, the reddish light of the companion remains visible (cf. Figure 3). Figure 4 also displays the hardness ratio plots “B/V” and “V/R”, which clearly show that the spectral energy distribution of the observed light changes significantly during (ingress and egress of) the eclipse (cf. §4 C). High time-resolution spectrally-resolved data such as those presented here provide strong constraints on, e.g., the geometry of the accretion flow and the location of the accretion spots on the surface of the white dwarf (e.g., Perryman et al. 2001).

## C. Spectra

Figure 5 shows the observed gain-corrected spectral energy distribution of UZ For (plus sky) outside and during the eclipse of the white dwarf (open squares and filled circles, respectively). It clearly confirms the inherent energy resolution of S-Cam, another key feature of the detector.

Extraction of intrinsic source spectra is a non-trivial exercise and requires a detailed characterization of the transmission of all components in the optical path, such as the atmosphere/night sky, the WHT mirrors and derotator, and the S-Cam unit itself. STJ devices nonetheless hold great promise as low-resolution spectro-photometers for, e.g., extragalactic astrophysics. A carefully designed observing and calibration program will ultimately allow for an efficient and reliable determination of “photometric redshifts” of high- $z$  galaxies (e.g., Perryman et al. 1993; Jakobsen 1999).

## D. Image location: differential atmospheric refraction

Atmospheric refraction causes a star at a zenith angle  $z$  to move towards the zenith by an amount  $\sim (n - 1) \tan(z)$ , where  $n$  is the index of refraction of the air layer near the Earth’s surface. As  $n$  not only varies with atmospheric pressure  $p$  and temperature  $T$  but also with wavelength  $\lambda$ , refraction makes every object appear as a little spectrum with the blue end towards the zenith and the red end towards the horizon. This effect is known as atmospheric dispersion or differential atmospheric refraction.

Atmospheric dispersion is clearly visible in the UZ For exposure (cf. Reynolds 2001): before the eclipse, i.e., during the first 10 minutes of the exposure, the mean centroid locations of red and blue counts (energy bands 1 and 3, respectively; §2 C and Table 1) differ by  $0.75''$ . The amount of atmospheric dispersion between energy bands 1 and 3 can also be predicted by using, e.g.,  $n = n_\lambda(p, T)$  from Filippenko (1982). Taking  $p = 771$  mbar and  $T = 14$  °C from

the night’s observing log, we estimate that differential refraction amounts to  $\sim [n_{\lambda=396 \text{ nm}} - n_{\lambda=573 \text{ nm}}] \tan(56^\circ) = 1.21''$ , which is significantly larger than the observed value. This prediction, however, depends sensitively on the assumed wavelengths, among other factors, and is best regarded as an order-of-magnitude estimate. The prediction of the position angle of the direction in which atmospheric dispersion operates on the S–Cam2 device, on the other hand, differs by less than  $3^\circ$  from the observed value, confirming the hypothesis that the image centroid shift with wavelength is due to atmospheric dispersion (cf. Figure 6).

## E. Image motion

Figure 6 shows the evolution of the centroid position of the “flat-fielded” and sky-subtracted counts (all energies; cf. Figure 1). An inspection of the data reveals that the image centroid is relatively stable, except for a number of discontinuous jumps. These features could, *a posteriori*, be related to (at least) four small manual guiding corrections at times 369, 609, 1 010, and 1 175 s (cf. Figures 1 and 7). Another feature in the image centroid location is (potentially) caused by differential refraction: during the eclipse, the source light becomes significantly less blue (e.g., Figures 4–5), with the result that the image centroid effectively moves in the direction towards the horizon (but see §4 F; cf. §4 D).

The image motion displayed in Figure 6, disregarding the artificial discontinuities mentioned above, is partly explained by telescope-induced tracking and guiding errors (cf. §4 G and Wilson et al. 1999). The main contribution, however, is due to atmospheric seeing. The expected root-mean-square image centroid variation due to seeing is (e.g., Lindegren 1979):

$$\sim \sqrt{0.2} \left( \frac{\lambda}{D} \right)^{1/6} \cdot \left( \frac{\lambda}{D_{\text{eff}}} \right)^{5/6} \sim 0.36'', \quad (6)$$

where  $D = 4.2 \text{ m}$  is the diameter of the aperture,  $\lambda = 479 \text{ nm}$  is the centroid wavelength (Table 1), and  $D_{\text{eff}} = 0.98 \lambda/\epsilon = 0.06 \text{ m}$  is Fried’s (1966) parameter;  $\epsilon$  is the full width at half maximum of the atmospheric seeing-induced point spread function ( $\sim 1.60''$  in this case; §4 F). During the exposure, the image centroid is thus expected to remain within  $\sim 1$  pixel, consistent with the observations.

## F. Image size: atmospheric seeing

The spatial resolution of S–Cam2 allows for the measurement not only of the centroid of the point spread function (PSF) in the focal plane (§§4 D and 4 E) but also of its size. As the combined effect of dome, mirror, and telescope seeing (due to tracking, focus, and aberration errors) is generally small for the WHT ( $\lesssim 0.30''$ ; e.g., Muñoz–Tuñón et al. 1998; Wilson et al. 1999), S–Cam2 can be used as an atmospheric seeing monitor. Seeing is usually expressed in terms of the full width at half maximum (FWHM, in units of arcseconds) of the time-averaged PSF (e.g., Coulman 1985). As the typical time scale of seeing is on the order of a few ms, a 1-s time binning generally allows for a sufficiently well-defined (i.e., smooth) PSF.

The top panels of Figure 7 show, for the “vertical” ( $X$ ) and “horizontal” ( $Y$ ) directions, the evolution of the centroid position (black dots; §4 E) and the interquartile range (grey dots) of the “flat-fielded” and sky-subtracted data (all energies). From these curves, the size of the region in which half of all counts is contained is readily obtained. If the functional form of the PSF is known (or specified), the size of this “interquartile area” can be directly related to the FWHM  $\epsilon$ , i.e., the amount of atmospheric seeing. The final step transforms  $\epsilon$  to units of arcseconds and corrects for zenith angle by multiplying with  $\cos^{3/5}(z)$ . The bottom panel of Figure 7 shows the evolution of the inferred seeing during the UZ For exposure assuming a Gaussian PSF; a Moffat (1969) function generally returns smaller estimates. The mean atmospheric seeing after the eclipse (see below) is  $1.60''$  ( $1.14''$  corrected for zenith angle). These estimates seem robust and sensible; unfortunately, an independent measurement of the seeing at the time of the observation is unavailable.

An uncertainty in the procedure outlined above is introduced by the use of polychromatic light, which is susceptible to differential atmospheric refraction (§4 D), for the definition of the interquartile area. In the case of UZ For, atmospheric dispersion operates, by coincidence, nearly along the diagonal direction on the device (e.g., Figure 6),



so that the PSF is elongated roughly equally strongly in the  $X$  and  $Y$  directions. The net result of this effect therefore is an overestimate of the size of the interquartile area, i.e., an overestimate of the inferred seeing, by  $\sim 10\%$ . The latter number was obtained by repeating the seeing analysis outlined above twice while restricting ourselves to semi-monochromatic light, i.e., “blue” and “red” counts. These tests also indicate that the mean interquartile ranges in  $X$  and  $Y$  for semi-monochromatic light may differ by  $\sim 10\%$  from each other, i.e., even the semi-monochromatic PSF is slightly asymmetric.

A crucial assumption in the procedure described above is that, given the selected time resolution, a sufficient number of source counts is available for a reliable definition of the image centroid and interquartile area. During the eclipse of the white dwarf by its faint companion this assumption is clearly violated at the selected time resolution (1 s; cf. Figure 3). This is evident, e.g., from the fact that the interquartile area seems significantly larger during than outside eclipse. We therefore conclude that the inferred seeing increase during the eclipse of the white dwarf may be spurious.

### G. Telescope pointing

The high speed and photon-counting and imaging capabilities of S-Cam2 enable the user to assess the impact on the final light curves of issues related to telescope tracking and guiding. The WHT has an altitude–azimuth mounting with two independent motors; its autoguider system operates at  $\sim 0.1$  Hz, i.e., tracking errors occurring at higher frequencies are uncorrected for.

**Pointing glitches:** The azimuth drive is known to suffer from pointing glitches (see <http://www.ing.iac.es/~crb/wht/tracking.html>). During these unpredictable events, the telescope pointing shoots off in azimuth after which it returns to its nominal position. The typical spatial amplitude of such glitches is several arcseconds; the typical duration is  $\sim 1.5$  s. An S-Cam2 observation of UZ For obtained during the Dec 1999 campaign, among others, contains two of these events (cf. Perryman et al. 2001). Figure 8 shows the pixel-integrated light curve of the source over a 5-s period spanning the first glitch, at a resolution of 5 ms; a higher time resolution is precluded by the low photon flux of UZ For.

Glitch “ingress” takes  $\sim 0.2$  s (time  $\sim 1500$ – $1700$ ), during which the image centroid is seen shooting off the device in the azimuthal direction (not shown). It takes  $\sim 0.3$  s for the WHT system to react to the loss of light (time  $\sim 1700$ – $2000$ ). In correcting for the glitch, the telescope initially “overshoots” (time  $\sim 2300$ ), after which it “bounces back” along the azimuthal direction (not shown) to its nominal position in  $\sim 1.0$  s (time  $\sim 2000$ – $3000$ ). The full duration of this glitch is  $\sim 1.5$  s. An S-Cam2 analysis of several of these features has revealed that their characteristics are very similar. It is not exactly known what triggers these pointing anomalies; large zenith angles could play a role ( $z \sim 58.4^\circ$  in this case).

**Pointing oscillations:** A remarkable finding was obtained during the Sep–Oct 2000 campaign when observing a non-variable circumpolar reference source for 300 s. During this exposure, the image centroid location showed an oscillatory pattern in the focal plane (Figure 9), unlikely to have been caused by random atmospheric phase fluctuations, i.e., seeing (§4E). The grey curves in Figure 9 show two independent sinusoidal fits to the image centroid data in the two “principal directions” altitude (elevation) and azimuth. Although this functional form is not necessarily the optimum choice, and has been chosen for illustrative purposes only, the fits provide a fair representation of the data. They suggest that the pointing oscillation has a period of  $\sim 38.1$  s ( $\sim 0.026$  Hz) and an amplitude of  $\sim 0.36''$ , 90% of which is in the altitude direction. The combination of the long period and relatively small amplitude of this phenomenon (as compared to a typical seeing disk with full width at half maximum of  $\sim 1''$ ) explains why similar oscillations have not been reported previously.

The large zenith angle of the source ( $z \sim 56.5^\circ$ ) might be a key factor in understanding the cause of the pointing oscillation. It is also interesting, in this respect, to recall that the WHT has a known structural oscillation frequency at  $\sim 2.7$  Hz. This resonance can have a significant effect if it is strongly excited, e.g., by wind buffeting of the telescope structure (see <http://www.ing.iac.es/Astronomy/development/hap/tracking.html>). During the observation discussed here, wind speed recordings were normal ( $\sim 30$ – $35$  km h $^{-1}$ ); the dome slit, however, was pointed to within  $\sim 30^\circ$  of the direction from which the wind was coming.

## 5. Discussion and conclusions

Even as recently as a decade ago, a high-speed optical photon counting detector with inherent energy resolution was an unknown concept. The development of the first generation of such an instrument, based on STJ technology, has now advanced to the stage where STJ-based imaging cameras containing dozens of pixels are starting to be operated. The high quality and potential of STJ data has been demonstrated, and first astrophysical results based on such measurements have been published (e.g., Perryman et al. 2001). With improved wavelength resolution in the future, STJ detectors, being operated as “multi-object redshift machines”, could significantly impact the field of extragalactic astronomy. Earlier and ongoing investigations aimed at evaluating an STJ-based instrument for the next-generation space telescope (NGST; e.g., Jakobsen 1999), as an interferometric fringe sensor for VLTI (R.S. Le Poole and W. Jaffe, private communication), and as a polarimeter for Subaru (M. Cropper, private communication) are merely the beginning of the integration of this novel detector into the forefront of astronomical thinking.

A number of STJ detectors in an array format, an STJ camera (S-Cam), generates four-dimensional data: photon arrival time, energy, and array element ( $X, Y$ ). The reduction and analysis of such data, typically several thousands of photons per second, is potentially involved and, while part of the high-energy data analysis culture, differs significantly from procedures adopted in a CCD environment. This paper describes an automated data reduction pipeline that is aimed at processing data generated by ESA’s S-Cam2 device. The implementation of the software is highly transparent and guarantees its portability to different platforms as well as an easy adaptation to future generation cameras. The pipeline takes care of energy calibration, barycentric time stamp correction, energy range selection, time binning, detector efficiency correction, atmospheric extinction correction, and sky background subtraction; a future version will also correct light-curve data for “noise” induced by the dead spaces between the array elements.

The analysis and interpretation of STJ data differs, in some respects, significantly from procedures adopted in CCD-based work. Differential atmospheric refraction, for example, is clearly observable with an STJ detector array and should be reckoned with. Atmosphere- or telescope-induced image motion on the device can be responsible, through a number of mechanisms, for spurious effects in light curves and hardness ratio plots. The interpretation of such data thus requires care. However, the sensitivity of S-Cam to such atmospheric effects offers, at the same time, the possibility to deepen our knowledge of the characteristics of atmospheric seeing, such as the relative importance of the wings of the seeing profile, the statistics of the amount of image smearing and motion, and wavelength-dependent effects. S-Cam data also provide useful diagnostics in relation to telescope pointing, tracking, and guiding.

Although revolutionary, the current generation of Tantalum-based STJ cameras is amenable to further development. Optical-STJ research within ESA is presently mainly driven towards the use of smaller energy gap/lower critical temperature (i.e., higher energy resolution) materials such as Hafnium, and towards larger format arrays (e.g., Verhoeve et al. 2001). Despite the fact that considerable technical challenges are to be faced, it is envisaged that a Hafnium-based detector array will ultimately allow for a wavelength resolution of 5 nm at 500 nm and count rates up to 10 000 photons per pixel. A space-borne version of such an instrument, with a response from 100 nm to 2  $\mu\text{m}$  and a detection efficiency larger than 80% throughout this range, would play a major role in future astronomy.

## ACKNOWLEDGMENTS

The research described in this paper is based on observations made with the William Herschel Telescope operated on the island of La Palma by the Isaac Newton Group (ING) in the Spanish Observatorio del Roque de los Muchachos of the Instituto de Astrofísica de Canarias. In ESTEC, N. Rando, J. Verveer, S. Andersson, D. Martin, and P. Verhoeve are thanked for their efforts in developing the S-Cam instrument. We are grateful to the ING staff for continued assistance, to the WHT time allocation committee for the generous assignment of engineering time for the first commissioning of S-Cam, and to our scientific collaborators involved in the analysis of the UZ For data, M. Cropper and G. Ramsay (Mullard Space Science Laboratory, University College London).

1. Benn C.R., Ellison S.L., 1998, *New Astronomy Reviews*, 42, 503
2. Coulman C.E., 1985, *ARA&A*, 23, 19
3. Delamere A., 1992, *ESA SP-356*, 111
4. Dravins D., Lindegren L., Mezey E., Young A.T., 1998, *PASP*, 110, 610
5. Filippenko A.V., 1982, *PASP*, 94, 715
6. Fried D.L., 1966, *J. Opt. Soc. Am.*, 56, 1372
7. Hasinger G., Snowden S.L., 1990, MPE Technical Note TN-ROS-ME-Za00/027 (Garching bei München: Max Planck Institut für extraterrestrische Physik)
8. Hayes D.S., Latham D.W., 1975, *ApJ*, 197, 593
9. Jakobsen P., 1999, in *Ultraviolet-optical space astronomy beyond HST*, ASP Conf. Ser., Vol. 164, eds J.A. Morse, J.M. Shull, A.L. Kinney, p. 397
10. King D.L., 1985, La Palma Technical Note, 31 (see also  
<http://www.ing.iac.es/Astronomy/observing/manuals/ps/tech-notes/tn031.pdf>,  
<http://www.ing.iac.es/Astronomy/observing/lpinfo/wlxt.html>, and  
[http://www.ing.iac.es/Astronomy/observing/INGinfo\\_calibration.html](http://www.ing.iac.es/Astronomy/observing/INGinfo_calibration.html))
11. Krisciunas K., Schaefer B.E., 1991, *PASP*, 103, 1033
12. Leinert Ch., et al., 1998, *A&AS*, 127, 1
13. Lindegren L., 1979, in *Proceedings of the colloquium "Modern astrometry"*, Vienna, Institut für Astronomie (Universitäts Sternwarte Wien), p. 197
14. Mazin B.A., Brunner R.J., 2000, *AJ*, 120, 2721
15. Mighell K.J., 1999, in *Precision CCD photometry*, ASP Conf. Ser., Vol. 189, eds E.R. Craine, D.L. Crawford, R.A. Tucker, p. 50
16. Moffat A.F.J., 1969, *A&A*, 3, 455
17. Muñoz-Tuñón C., Varela A.M., Mahoney T., 1998, *New Astronomy Reviews*, 42, 409
18. Peacock A., Verhoeff P., Rando N., Perryman M.A.C., Taylor B.G., Jakobsen P., 1997, *A&AS*, 123, 581
19. Peacock A., Verhoeff P., Rando N., Erd C., Bavdaz M., Taylor B.G., Perez D., 1998, *A&AS*, 127, 497
20. Perryman M.A.C., Foden C.L., Peacock A., 1993, *Nuclear instruments and methods in physics research (section A)*, 325, 319
21. Perryman M.A.C., Favata F., Peacock A., Rando N., Taylor B.G., 1999, *A&A*, 346, L30
22. Perryman M.A.C., Cropper M., Ramsay G., Favata F., Peacock A., Rando N., Reynolds A.P., *MNRAS*, 2001, 324, 899
23. Reynolds A.P., 2001, [http://astro.estec.esa.nl/SA-general/Research/Detectors\\_and\\_optics/detectors\\_scam-5.html](http://astro.estec.esa.nl/SA-general/Research/Detectors_and_optics/detectors_scam-5.html)
24. Stetson P.B., 1990, *PASP*, 102, 932
25. Stickland D.J., Lloyd C., Pike C.D., Walker E.N., 1987, *The Observatory*, 107, 74
26. Verhoeff P., Rando N., Peacock A., Martin D., den Hartog R., 2001, this volume (see also  
[http://astro.estec.esa.nl/SA-general/Research/Detectors\\_and\\_optics/home.html](http://astro.estec.esa.nl/SA-general/Research/Detectors_and_optics/home.html))
27. Wilson R.W., O'Mahony N., Packham C., Azzaro M., 1999, *MNRAS*, 309, 379
28. Young A.T., 1967, *AJ*, 72, 747
29. Young A.T., et al., 1991, *PASP*, 103, 221

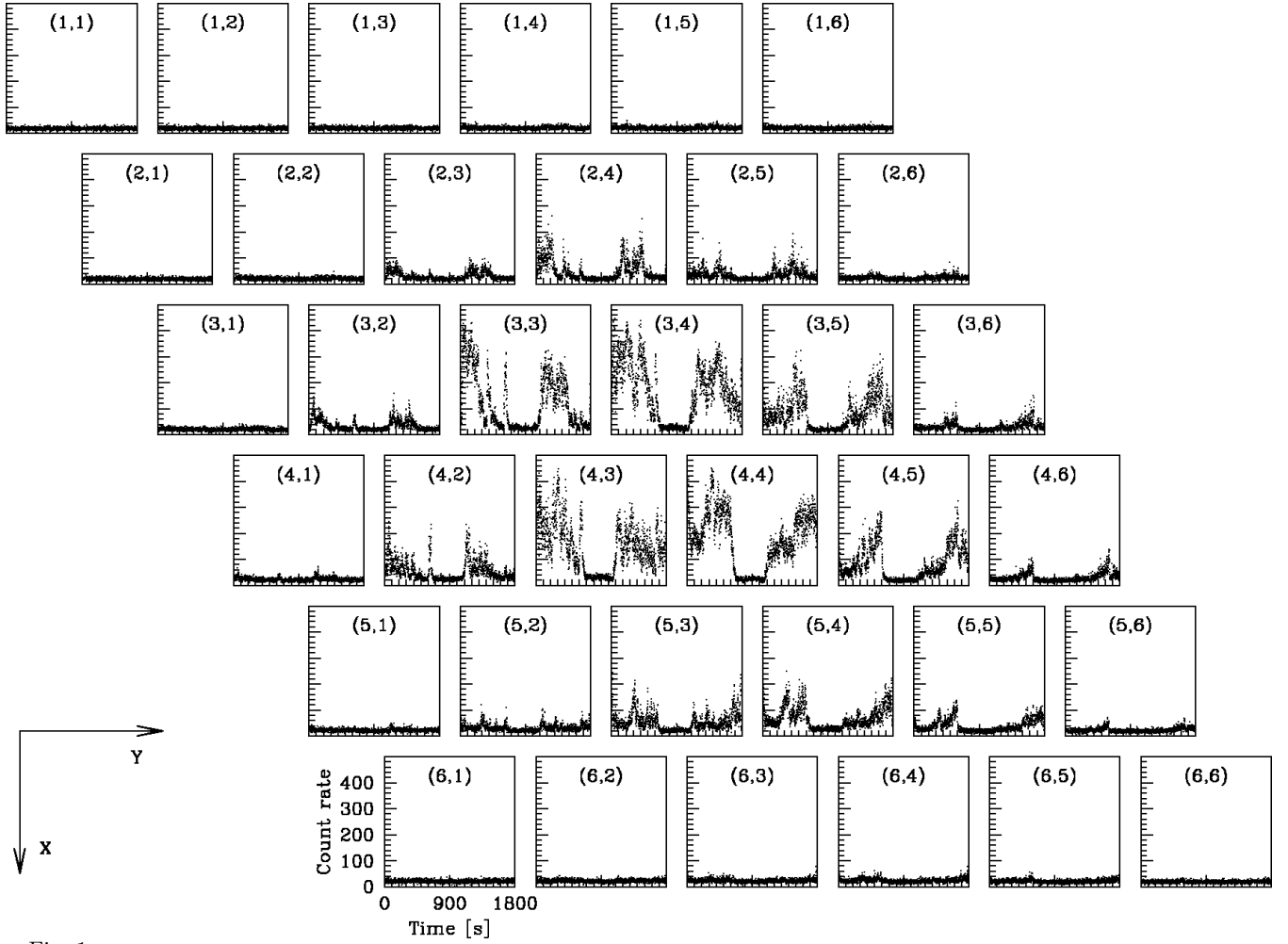


Fig. 1.

S-Cam2 array layout and pixel-selected light curves of UZ For. The panels represent the genuine architecture of the  $6 \times 6$  array elements ( $X, Y$ ) in the focal plane. One pixel is  $25 \times 25 \mu\text{m}^2$  in size and spans  $\sim 0.6'' \times 0.6''$  on the sky. Pixels are not directly adjacent: inter-junction dead spaces are  $\sim 4 \mu\text{m}$ . The data displayed in the pixels are light curves (at a 1-s time resolution for all energies; §§2 C–2 D) after gain correction (§2 A), but before “flat fielding” (§2 E), extinction correction (§2 F), and sky subtraction (§2 G; cf. Figure 3). Count rates are given in units of photons per second; the time axis is relative to the start of the exposure (cf. §2 B). The pronounced dip in the light curves roughly halfway the observation indicates an eclipse of the white dwarf in the UZ For binary system (§4 B). The data clearly show that, during the exposure, atmospheric seeing has moved the image around over the array (§4 E). A number of sharp features, e.g., around time = 609 s, corresponds to manual guiding corrections (§4 E).

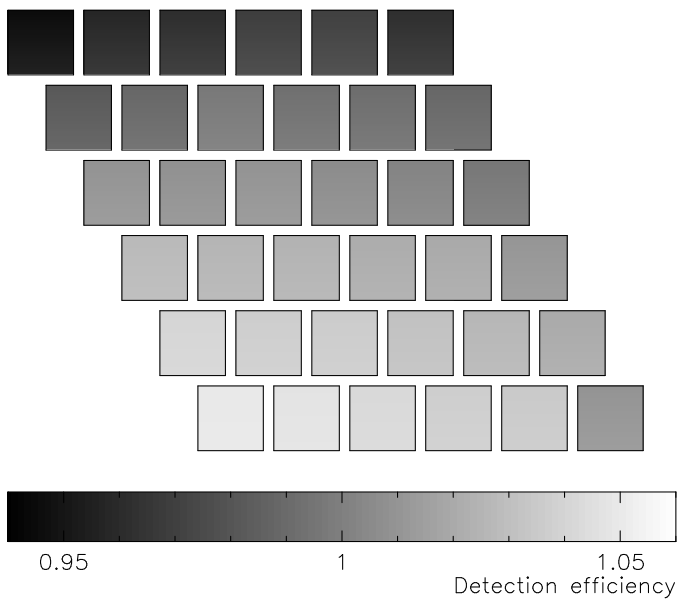


Fig. 2.  
 Grey-scale representation of the detector efficiency map. The responsivity of the reference pixel ( $X, Y = 3, 1$ ; the first junction in the third row; cf. Figure 1) was fixed at unity. The apparently smooth structure in the map is most likely due to vignetting caused by the relay optics including the infrared photon blocking filters (§2 E).

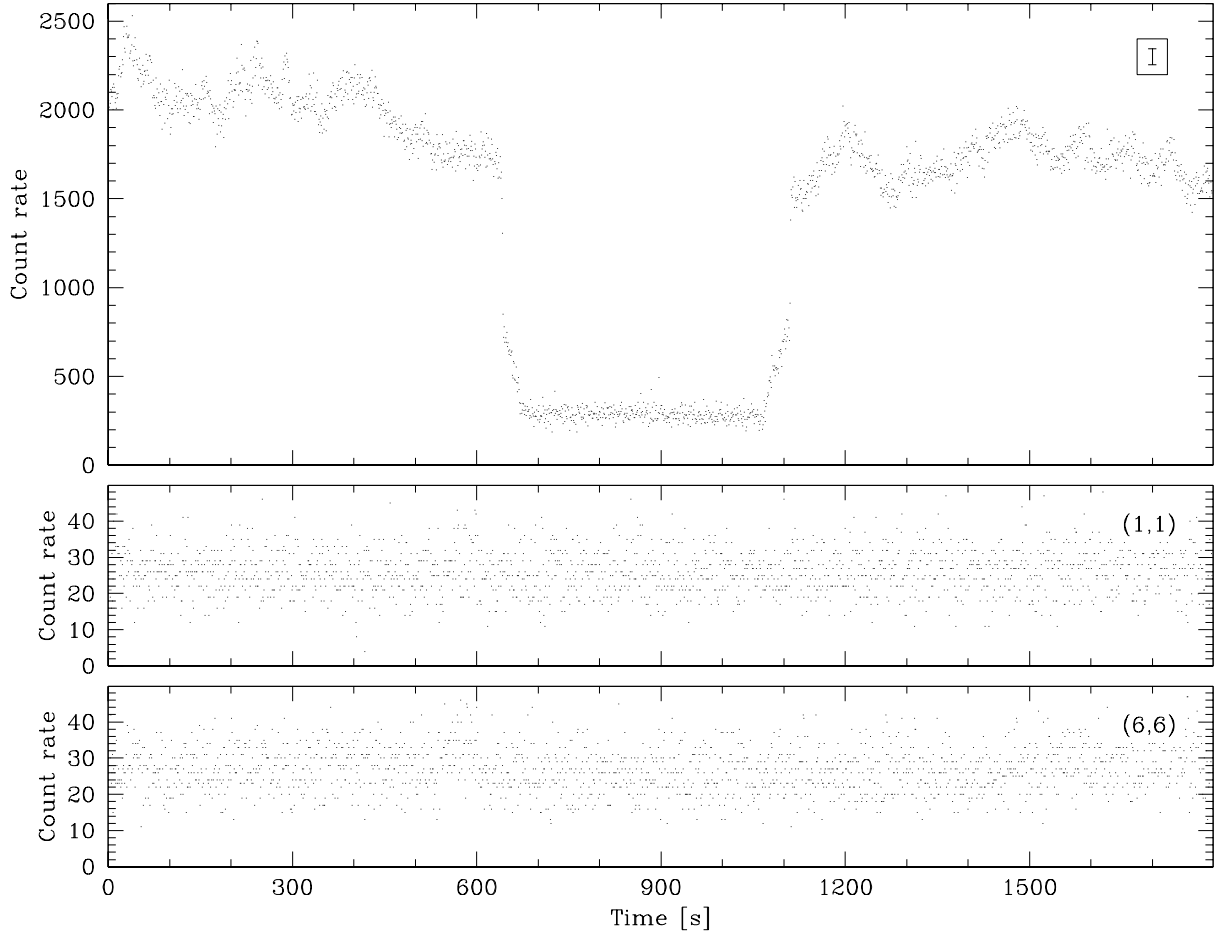


Fig. 3.

Background subtraction. *Top panel*: “flat-fielded” and sky-subtracted pixel-integrated light curve for UZ For (at a 1-s time resolution; count rate in photons per second). The sky contribution was estimated at  $6 \times 6 \cdot 26.5 = 954$  counts  $s^{-1}$ , independent of time (see below; cf. §2 G). The error bar in the top right corner roughly indicates the expected Poisson noise for a count rate of 2000 counts  $s^{-1}$  (§3 A). During the eclipse of the white dwarf, its faint companion accounts for  $\sim 300$  photons  $s^{-1}$ . The pixel-integrated light curve does not reveal traces of the manual guiding corrections visible in the pixel-selected data (Figure 1). *Bottom panels*: light curves of the corner pixels ( $X, Y = 1, 1$ ) and  $(6, 6)$  (count rates in photons per second per pixel). S-Cam2 is a photon counting detector: as a result, count rates take on integer values exclusively. The mean time-averaged count rate of the two pixels is  $26.5$  photons  $s^{-1}$  pixel $^{-1}$ ; this value is assumed to represent the sky background intensity. Around time  $\sim 550$  s, the image center slowly moves towards pixel  $(6, 6)$ , as evident from the slightly enhanced count rate (bottom panel); a manual guiding correction at time = 609 s corrects for this drift (§4 E and Figure 6).

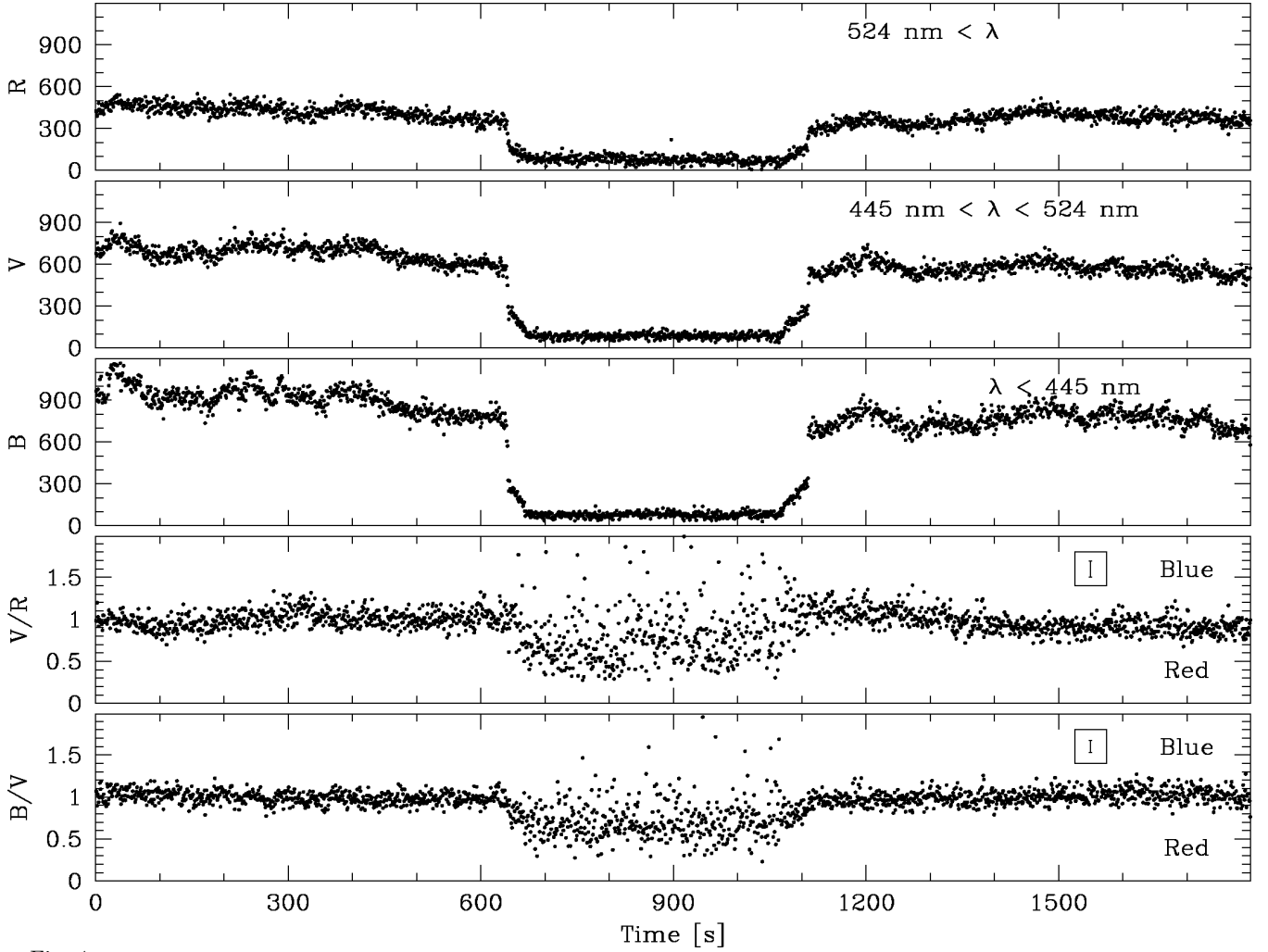


Fig. 4.

Top three panels: “flat-fielded” and sky-subtracted pixel-integrated light curves of UZ For in a low-, medium-, and high-energy band, respectively. For ease of reference, these bands are referred to as red (“R”;  $E_0-E_{98}$ ;  $\lambda > 524$  nm), yellow (“V”;  $E_{99}-E_{116}$ ;  $445 \text{ nm} \leq \lambda \leq 524$  nm), and blue (“B”;  $E_{117}-E_{255}$ ;  $\lambda < 445$  nm; §2 C and Table 1). The energy bands are defined such that they contain (roughly) equal amounts of counts; later correction for atmospheric extinction (§2 F) leads to a significantly uneven distribution. During the eclipse of the white dwarf, the reddish light of the companion remains visible (cf. Figures 3 and 5). Bottom two panels: the colour ratios “V/R” and “B/V” (after an arbitrary vertical scaling); lower values indicate a redder colour. The error bars indicate the expected noise due to photon statistics for artificial yet representative count rates of 400, 600, and 800 counts  $\text{s}^{-1}$  for “R”, “V”, and “B”, respectively. The spectral energy distribution of the observed light changes significantly during the eclipse of the white dwarf (cf. §4 C and Figure 5).

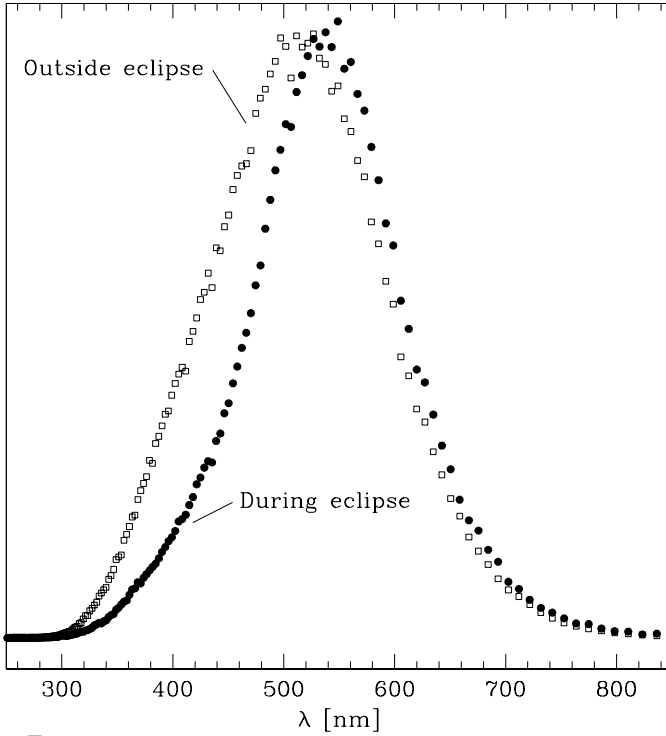


Fig. 5.

Gain-corrected and time-integrated spectral energy distributions, before sky subtraction, during and outside the eclipse of the white dwarf in UZ For (filled circles and open squares, respectively). Wavelengths were obtained from energy channels by means of equation 3. The vertical axis denotes counts per energy channel on an arbitrary scale. The sky and faint red companion contribute  $\sim 1000$  and  $\sim 300$  photons  $s^{-1}$  to the total flux, respectively; the hot white dwarf accounts for  $\sim 1500$  photons  $s^{-1}$  (e.g., Figure 3). The spectrum outside eclipse is bluish, but with a significant contribution from the sky; the spectrum during eclipse is dominated by sky photons. The spectra nonetheless confirm the inherent energy resolution of optical STJ detectors. “Noisy” features are due to the analogue-to-digital conversion electronics and can be corrected during data processing. The shape of the observed spectra can be understood by convolving the intrinsic spectrum with the atmosphere, WHT mirrors and derotator, S-Cam optics, detector efficiency, and detector energy resolution. The blue cutoff at  $\sim 310$  nm is primarily due to the atmosphere; the cutoff at  $\sim 720$  nm (taking the energy resolution of S-Cam2 into account) is due to the infrared photon blocking filters (§2 E).



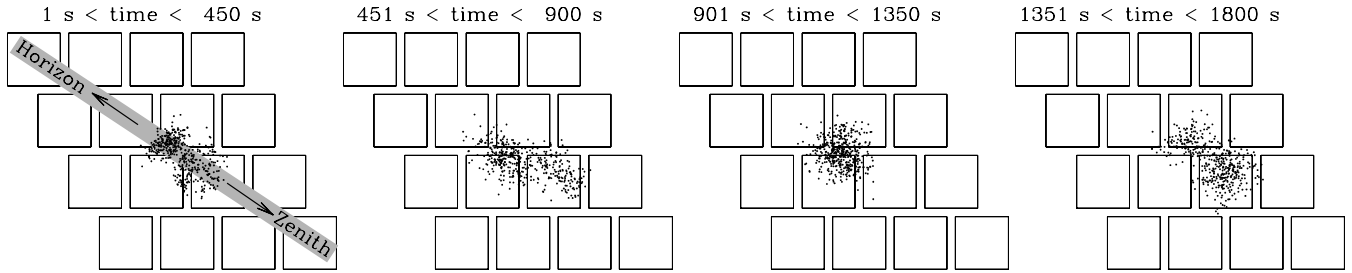


Fig. 6.

UZ For image centroid motion in the focal plane during four equal-length time spans; only the 16 central pixels are shown. Taking inter-junction dead spaces into account, one pixel corresponds to  $\sim 0.7'' \times 0.7''$  in this figure. The 1-s time resolution data correspond to the “flat-fielded” and sky-subtracted counts (all energies). The left panel indicates, for the UZ For observation discussed here, the direction towards the zenith and the horizon. Outside eclipse (see below), the observed mean centroid displacement between any pair of consecutive 1-s time bins is  $\sim 0.17$  pixel  $\sim 0.12''$ . The image motion can be understood as the superposition of (i) random components due to atmospheric seeing (root-mean-square centroid variation  $\sim 0.36''$ ) and telescope-induced guiding and tracking errors and (ii) a number of jumps due to manual guiding corrections (times 369, 609, 1010, and 1175 s; §4E; cf. Figures 1 and 7). During the eclipse of the white dwarf ( $640 \text{ s} \lesssim \text{time} \lesssim 1120 \text{ s}$ ), the count rate of the faint companion ( $\sim 300 \text{ photons s}^{-1}$ ) is too low to allow for a reliable determination of the centroid location at the selected binning period (cf. §4F).

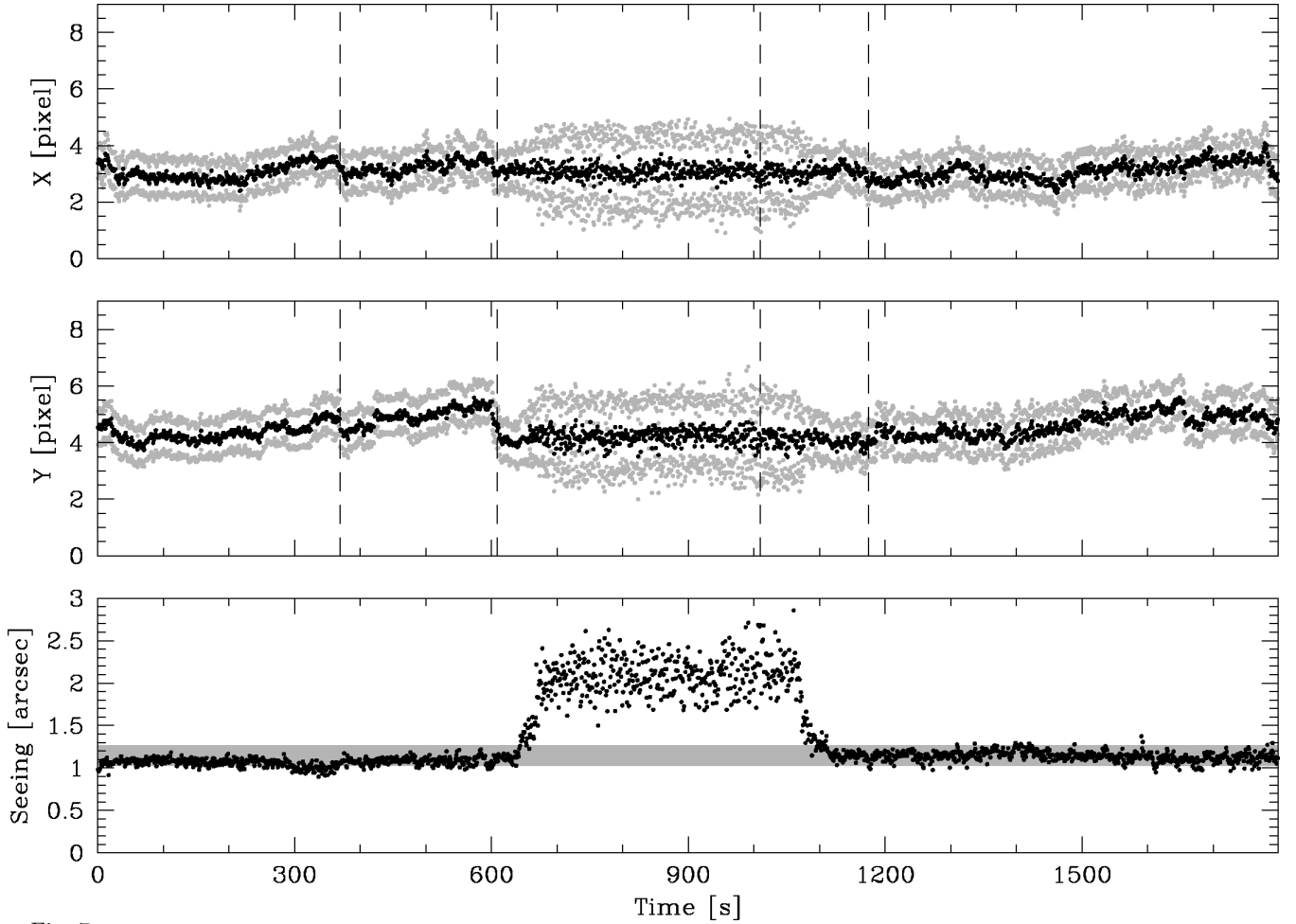


Fig. 7.

Atmospheric seeing analysis for UZ For. *Top panel:* the evolution of the centroid position (black dots) and the corresponding interquartile range (grey dots) in the  $X$  direction (the “vertical” direction on the device; cf. Figure 1). The data, at a 1-s time resolution, refer to the “flat-fielded” and sky-subtracted counts (all energies). During the eclipse of the white dwarf, the number of source counts from the faint companion is insufficient to determine the centroid and interquartile range reliably at the selected time resolution (§4F). Manual guiding corrections were made around times 369, 609, 1010, and 1175 s; these explain discontinuities in the centroid evolution (cf. Figure 6). *Second panel:* as the top panel, but for the “horizontal”  $Y$  direction on the device. *Bottom panel:* inferred seeing estimates with time (corrected for zenith angle) assuming a Gaussian point spread function (§4F). The grey band denotes the mean atmospheric seeing estimate during the last 700 s of the exposure:  $\epsilon = 1.14''$  ( $1.60''$  uncorrected for zenith angle). The increased seeing during the eclipse is spurious (§4F).

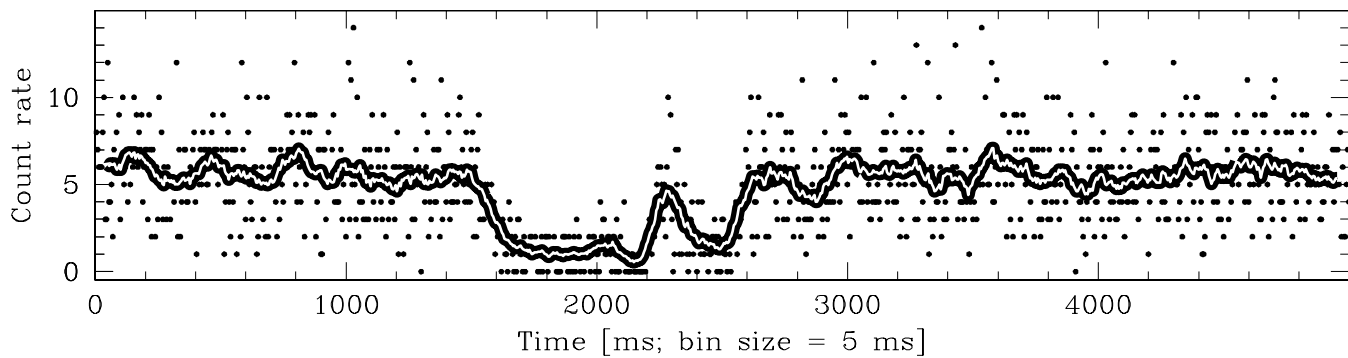


Fig. 8. Pointing glitch in the UZ For exposure (§4G). The dots show the light curve of the source (all energies), before extinction correction and background subtraction, over a 5-s period at a time resolution of 5 ms; the ordinate is in units of photons per time bin. The curve is the running average of the count rate over 20 time bins, i.e., 0.1 s. Glitch “ingress” runs from time  $\sim 1500$  to  $\sim 1700$ . During  $\sim 0.3$  s following “ingress”, S-Cam2 registers  $\sim 0$ – $2$  sky photons per 5 ms time bin, compared to  $\sim 5$  counts per time bin normally. Glitch “egress” runs from time  $\sim 2000$  to  $\sim 3000$ . The spatial resolution of S-Cam2 reveals that the dis- and re-appearance of source light takes place along the azimuthal direction (not shown).

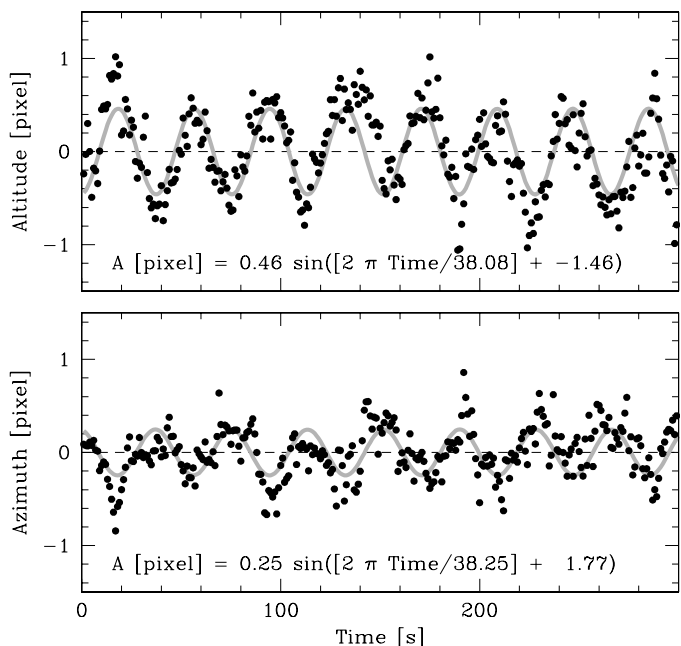


Fig. 9. Pointing oscillation (§4 G). The dots show the evolution of the image centroid location with time, at a 1-s resolution, for the altitude (elevation; *top panel*) and azimuth directions (*bottom panel*). The ordinates denote location in the focal plane in units of pixels (one pixel is  $\sim 0.7''$ , after correcting for inter-pixel dead spaces). The grey sine-curves are two independent fits to the data; the best-fit parameters are indicated in the panels (amplitudes in units of pixels, time and periods in units of seconds, and phases in radians). The fits provide a fair representation of the observations, given the facts (i) that the chosen functional form does not necessarily have a physical meaning, and (ii) that a random image motion component due to seeing is also present in the data (§4 E).

Table 1.

Energy range selection and atmospheric extinction correction for UZ For (§§2 C and 4D). The first column denotes the energy band (0 for all energies); the second column schematically denotes its colour. The third and fifth columns denote the lower and upper energy channels defining the energy band; the fourth and sixth columns denote its centroid channel and wavelength, respectively (equation 3). The last column provides the corresponding mean extinction coefficient  $k_\lambda$  valid for La Palma. The value for the exposure containing all counts (energy band 0) is the mean of the coefficients of the energy-selected sub-exposures;  $k_\lambda$  corresponding to the centroid wavelength ( $\lambda = 479$  nm) is  $0.1434 \text{ mag airmass}^{-1}$ . The count rate correction factors are  $10^{0.4k_\lambda \cdot A}$ ; the airmass  $A$  changes from 1.75 to 1.83 during this observation.

Energy band	“colour”	$E_{\text{low}}$	$E_{\text{centroid}}$	$E_{\text{high}}$	$\lambda_{\text{centroid}}$ nm	$k_\lambda$ mag airmass $^{-1}$
0	white	0	108	255	479	0.1798
1	red	0	90	98	573	0.0993
2	yellow	99	106	116	488	0.1345
3	blue	117	131	255	396	0.3056